Chemical Science

ROYAL SOCIETY OF CHEMISTRY

EDGE ARTICLE

View Article Online
View Journal | View Issue

Cite this: *Chem. Sci.*, 2025, **16**, 22565

All publication charges for this article have been paid for by the Royal Society of Chemistry

Surface chemistry regulation of conductive two-dimensional nanosheets with highly pseudocapacitive covalent groups for a high-performance flexible asymmetric microsupercapacitor

Yuanming Wang, *[a] Jinlong Wu,[a] Jiayue Dong,[a] Xiaoxu Xu,[a] Huan Song,[a] Libei Yuan,[b] Xiaolong Li*[c] and Zhaoqing Lu *[a]

Flexible microsupercapacitors are attracting much more attention for use in miniature energy storage devices due to their attractive electrochemical characteristics. However, it is difficult to achieve high energy density and long-term stability at the same time due to a lack of suitable high-specific-energy materials. Herein, an innovative asymmetric microsupercapacitor is obtained by the highly efficient surface chemistry regulation of conductive two-dimensional nanosheets of both graphene and MXene with highly active covalent groups. To optimize the positive graphene material, graphene oxide powder is first employed, undergoing a fast expansion and exfoliation process *via* water molecule explosive vaporization. Then, the conductive graphene sheet layer with a high specific surface area is oxidized selectively by acid treatment to introduce pseudocapacitive groups at an optimized proportion and density (more –COOH and less –OH), and this is labelled as expanded-and-oxidized graphene (EOG). To optimize the negative MXene material, delaminated MXene nanosheets undergo hydroxyl substitution through alkalization, and the two-dimensional (2D) lamellae become wrinkled using coulombic attraction for fast intercalation pseudocapacitance, and this is labelled as wrinkled-and-hydroxylated MXene (WOM). Through surface chemistry modification and all-pseudocapacitive 2D structure design, flexible EOG and WOM composite electrodes exhibit capacities of 382 F g^{-1} and 550 F g^{-1}, respectively, and have remarkable stability. An assembled proton-type solid-state microsupercapacitor with a voltage window of 1.5 V readily achieves an energy density of 47.25 mW h cm^{-3} (23.62 W h kg^{-1}) at a power density of 1900.55 mW cm^{-3} (950.27 W kg^{-1}), with high capacity retention of 86.8% after 8000 cycles. This work shows a well-designed microdevice with flexible and integrable properties based on 2D microstructure engineering for use in flexible electronics.

Received 14th September 2025
Accepted 15th October 2025

DOI: 10.1039/d5sc07080e

rsc.li/chemical-science

1. Introduction

Flexible electronic products have become more and more common and popular in our daily lives due to their attractive traits, such as their wearability, portability and smart characteristics, and they are used for artificial intelligence, health monitoring, mobile communications, and so on.[1,2] This has greatly accelerated the development of electrochemical energy storage devices towards the goal of miniaturization and system integration in order to adapt to situations where volume and space are limited in electronic components.[3,4] Among these devices, planar microsupercapacitors have the obvious advantages of a fast charging/discharging process, long lifespan, simple manufacturing processes and low operation costs, enabling them to be strongly competitive candidates. To date, microsupercapacitors have made significant progress in terms of practical applications due to the development of advanced manufacturing technologies such as silk-screen printing, 3D printing, laser engraving, mask assistance and so on.[5–7] Utilizing solution processing routes to produce microsupercapacitors is a cost-effective and high-efficiency method that has low equipment requirements, thereby showing wide application and promise.[8] When using this approach, the interior properties of electrode materials become significantly

[a]*College of Bioresources Chemical and Materials Engineering, Shaanxi Provincial Key Laboratory of Papermaking Technology and Specialty Paper Development, National Demonstration Center for Experimental Light Chemistry Engineering Education, Shaanxi University of Science & Technology, Xi'an 710021, P.R. China. E-mail: yminghit@sust.edu.cn; luzhaoqing302@163.com*

[b]*Institute for Superconducting and Electronic Materials, Australian Institute for Innovative Materials, University of Wollongong, Wollongong, New South Wales 2522, Australia*

[c]*State Key Laboratory of Advanced Polymer Materials, Polymer Research Institute, Sichuan University, Chengdu 610065, P.R. China. E-mail: lixiaolong1038@163.com*

important, and they need to meet the requirements of solution processing and film-forming while having flexibility and high energy output at the same time. However, the challenge is that there is a limited supply of materials with these properties and it is difficult to combine energy density with long-term stability in most cases.[9–11]

Conductive two-dimensional (2D) nanomaterials have attracted widespread interest for use in flexible micro-supercapacitors due to their exceptional attributes, including high specific surface areas, tunable surface functional groups, and excellent electrical conductivity.[12–14] As an emerging 2D material, the MXene family, whose components can be described by the general formula $M_{n+1}X_nT_x$ ($n = 1$–3), has huge potential applications in the energy storage field.[15] It is worth noting that $Ti_3C_2T_x$ MXene film material, where T_x represents the surface terminal functional groups –OH, –O, and –F, has a mass-based specific capacitance of up to 380 F g^{-1} and a volume-based specific capacitance of up to 1500 F cm^{-3} in acidic electrolyte.[16] To our knowledge, $Ti_3C_2T_x$ MXene remains the most conductive member of the MXene family, and film materials fabricated by using MXene nanosheets with large horizontal dimensions and large-scale blade coating methods can achieve electronic conductivity of up to 15 100 S cm^{-1}.[17] Meanwhile, $Ti_3C_2T_x$ MXene exhibits excellent stability in acidic environments, which greatly promotes the booming development of MXene-based microsupercapacitors, especially proton-type supercapacitors.[18] This is because the charge carriers in proton-type supercapacitors have the smallest ionic radius, realizing rapid ion diffusion kinetics; these are more prominent in solid-state systems than other ions, favoring the achievement of both high rate capability and high energy density.[19] Although MXene-based microsupercapacitors can achieve much higher energy density in an asymmetric configuration due to the wider operating voltage window, a challenge still exists due to the lack of suitable positive 2D materials that can be matched with MXene in terms of processing attributes and electrochemical properties; this is needed in order to break through the performance bottleneck relating to MXene-based flexible microsupercapacitors.[20,21]

Graphene, a typical 2D layered nanocarbon material, has a wide range of applications in supercapacitors due to its high theoretical capacity value of up to 550 F g^{-1}, extremely high electrical conductivity and outstanding chemical stability.[13] Based on these merits, it is considered to be an ideal choice as a positive conductive 2D material to match with MXene in the same acidic environment to create an asymmetric system with a large operating voltage window and excellent electrochemical behavior.[22] However, given the strong π–π and van der Waals interactions between graphene layers, graphene is prone to severe agglomeration during electrode preparation, resulting in a low specific surface area and specific capacitance.[23] Also, the energy storage mechanism of pristine graphene is predominantly governed by electric double-layer capacitance, which brings about relatively lower capacitance because of the limited pseudocapacitive contribution.[24] To alleviate the less electrochemically active surface of graphene, surface chemical modification is widely regarded as one of the most effective regulation approaches.[25,26] The capacitive performance of graphene can be enhanced through doping with various heteroatoms, such as O, N, P and S elements. Heteroatom doping can improve the electronic properties of graphene and introduce additional pseudocapacitance,[27] thereby increasing the specific capacitance. Besides, some research and computational simulations have shown that a certain amount of oxygen-containing functional groups on the carbon material surface can obviously improve the pseudocapacitance.[28] However, introducing such groups onto graphene remains challenging due to the inert nature of the carbon basal planes and the limited surface chemical reactivity.[29] Also, it is difficult to precisely regulate the type and density of these functional groups through current methods for solution processing.[30] However, once a pseudocapacitive 2D graphene positive electrode is able to cooperate with a pseudocapacitive 2D MXene negative electrode, allowing the construction of a proton-type solid-state asymmetric microsupercapacitor, the behavior is expected to be considerably attractive from many aspects by virtue of the advantages of all-pseudocapacitive 2D materials.

In this work, an innovative proton-type solid-state asymmetric microsupercapacitor is realized for the first time by employing the all-pseudocapacitive 2D materials of chemically modified graphene and MXene lamella as the cathode and anode materials through acid oxidization and alkaline optimization methods, respectively. For the fabrication of chemically modified graphene, graphene oxide (GO) is first subjected to a fast expansion and exfoliation process *via* water molecule explosion vaporization. Due to the exposure of a large number of carbon basal planes, a mixed acid oxidation process can be carried out to selectively produce pseudocapacitive oxygen-containing functional groups (such as more –COOH and less –OH) at an optimized proportion and density by regulating the oxidization process of expanded graphene (EG). Thus, novel expanded-and-oxidized graphene (EOG) is formed with a highly pseudocapacitive wrinkled surface, good dispersity and wettability for facile solution processing. For the fabrication of chemically modified MXene, delaminated MXene nanosheets undergo alkalization treatment to regulate the surface termini by introducing more –OH functional groups for redox reactions. Meanwhile, the 2D lamellae become wrinkled using coulombic attraction from metal potassium ions for fast ion diffusion; therefore wrinkled-and-hydroxylated MXene (WOM) can be formed by controlling the alkaline conditions. In addition, to further enhance the electrochemical performance and flexibility of the EOG and WOM electrodes, electrochemically delaminated graphene (EDG) is incorporated because of tight face-to-face connection and excellent electron conduction. The resulting flexible composite positive EOG film (CEOG) and negative WOM film (CWOM) electrodes can achieve high specific capacitances of 382 F g^{-1} and 550 F g^{-1}, respectively, and are able to endure long-term stability testing. Benefiting from the synergistic design based on surface chemistry engineering and the all-pseudocapacitive structural configuration, the assembled solid-state proton microsupercapacitor with good flexibility and integrated features exhibits a high energy density of 47.25 mW h cm^{-3} (23.62 W h kg^{-1}) at a power density of 1900.55

mW cm^{-3} (950.27 W kg^{-1}) in an expanded voltage window of 1.5 V, and high capacity retention of 86.8% is achieved after 8000 charging/discharging cycles. The work highlights the potential of conductive 2D materials upon rationally regulating their active pseudocapacitive surface and provides new solutions for high-performance microsized energy storage devices.

2. Experimental section

2.1 Materials

Graphene oxide powder (GO, 99%) was obtained from Shanghai Macklin Biochemical Co, Ltd (China). MAX (Ti_3AlC_2, 99%) was acquired from Laizhou Kai Kai Ceramic Materials Co., Ltd. Lithium fluoride (LiF, 99%), ammonium chloride (NH_4Cl, AR), polyvinyl alcohol (PVA, 99%), and glutaraldehyde (50% in H_2O, AR) were supplied by the Shanghai Aladdin Bio-Chem Technology Co, Ltd (China). Potassium hydroxide (KOH, AR), hydrochloric acid (HCl, AR), sulfuric acid (H_2SO_4, AR) and nitric acid (HNO_3, AR) were obtained from Shanghai Sinopharm Chemical Reagent Co, Ltd (China). All reagents were used as received without further purification.

2.2 Synthesis of EDG nanosheets

Graphite plates were exfoliated using an electrochemical approach. Specifically, a piece of graphite paper (1 cm (length) × 1 cm (width) × 0.5 mm (thickness)) served as the working electrode, while a platinum (Pt) plate (1 cm (length) × 1 cm (width)) was employed as the inert counter electrode. Electrochemical exfoliation was performed in a mixed electrolyte solution containing 0.1 mol L^{-1} sulfuric acid (H_2SO_4) and 0.02 mol L^{-1} ammonium chloride (NH_4Cl). A constant external voltage of 20 V was applied to the system to drive the exfoliation process in constant voltage mode. Throughout exfoliation, the electrolyte was subjected to constant magnetic stirring to enhance mass transfer. Upon completion of graphite exfoliation, the detached graphene layers were collected and repeatedly washed with deionized (DI) water. Finally, the washed electrochemically delaminated graphite (EDG) was dispersed in deionized water and subjected to ultrasonication to form a stable ED dispersion.

2.3 Synthesis of EG and EOG nanosheets

Initially, a predetermined amount of graphene oxide (GO) was mixed with deionized water under stirring to form a homogeneous GO paste. This GO paste was then subjected to cold pressing at 15 MPa, resulting in the formation of a compact GO cake. Subsequently, the GO cake was rapidly expanded using a steam shock method (flash evaporation). A sealed aluminum container was used to store the GO cake and it was promptly heated by utilizing a burning alcohol lamp. The water molecules in the GO interlay instantaneously exploded due to the rapid high-temperature vaporization, inducing expansion and reduction reactions, thereby producing conductive expanded graphene (EG) lamellae in abundance.

Following expansion, EG underwent surface functionalization by a facile acid oxidization method. Specifically, 200 mg of EG was added to a predetermined volume of a concentrated acid mixture with a volume ratio of 3 : 1 of concentrated H_2SO_4 and HNO_3. Crucially, the acid mixture was prepared and maintained in an ice-water bath to ensure complete cooling prior to the addition of EG powder. The substance was then treated within this cooled strong acid mixture to yield expanded-and-oxidized graphene (EOG). After functionalization for specified durations (3 h, 6 h, and 9 h), EOG dispersed in the strong acid solution was collected thorough water washing *via* repeated centrifugation and redispersion cycles. Finally, washed EOG was ultrasonicated in deionized water to form a uniform dispersion for subsequent use.

2.4 Synthesis of delaminated $Ti_3C_2T_x$ MXene and wrinkled MXene-OH (WOM) nanosheets

Initially, 5 g of lithium fluoride (LiF) was dispersed into 30 mL of 9 mol L^{-1} hydrochloric acid (HCl) solution. 5 g of MAX phase powder was gradually added to the above etchant solution and reacted at 30 °C for 18 hours. The etched MAX phase suspension was centrifuged at 3500 rpm and repeatedly washed until the pH of the supernatant approached neutrality. The resulting precipitate was dispersed in deionized water and agitated for 30 minutes, followed by centrifugation at 3500 rpm for 1 hour to obtain a dark green MXene dispersion (8 mg mL^{-1}). Subsequently, a predetermined volume of the MXene dispersion was subjected to alkalization treatment for surface functionalization. Potassium hydroxide (KOH) was added at twice the mass of the MXene solid content in the dispersion and this was allowed to react for 6 hours. This process yielded hydroxyl-functionalized MXene, denoted as MXene-OH, which was wrinkled due to the coulombic attraction involving metal potassium ions, so wrinkled-and-hydroxylated MXene (WOM) was synthesized based on this process.

2.5 Preparation of free-standing composite film CEOG and CWOM electrodes

To further enhance the electrode electrochemical performance and flexibility, highly conductive EDG was introduced into EOG and WOM materials to produce composite free-standing film electrodes, denoted as CEOG and CWOM film electrodes, respectively. Firstly, EDG and EOG solutions were mixed at predetermined mass ratios and stirred using a magnetic stirrer to obtain homogeneous mixed solutions. Subsequently, the mixed solutions were subjected to vacuum filtration through cellulose filter membranes with a pore size of 0.22 μm. The resulting filter cakes were then vacuum-dried to yield free-standing CEOG film electrodes. A series of film electrodes with varying EDG mass percentages was prepared, specifically with EOG : EDG mass ratios of 9 : 1, 8 : 2, and 7 : 3. These free-standing CEOG film electrodes exhibited a final mass loading of ~2 mg cm^{-2} based on the total mass. For the preparation of the CWOM film electrode, WOG and EDG were mixed at a mass ratio of 7 : 3. Then the mixture dispersion was subjected to vacuum-assisted filtration, yielding a free-standing composite film with a mass loading of ~1 mg cm^{-2}.

2.6 Preparation of a proton-type solid-state asymmetric microsupercapacitor (AMSC)

Initially, a tailored interdigital mask mold was pressed onto a cellulose filter membrane (pore size: 0.22 μm) to carry out solution processing by vacuum-assisted filtration. Subsequently, 2.5 mL of the positive material dispersion (7 : 3 weight ratio of EOG : EDG, 0.5 mg mL^{-1}) was introduced to one side of the interdigital channels, while 1.5 mL of the negative material dispersion (7 : 3 weight ratio of WOG : EDG, 0.5 mg mL^{-1}) was applied to the opposing side. Vacuum filtration was then performed on the dispersions to form the interdigital microelectrodes. Following mask removal, the as-prepared interdigital microelectrode composites readily transferred to the polyimide (PI) substrate due to strong adhesion. Using this method, an array of microelectrodes could be interconnected on the PI substrate. Finally, a PVA/H_2SO_4 hydrogel electrolyte was coated and solidified onto the microdevice to form a solid-state asymmetric microsupercapacitor. The hydrogel electrolyte was typically prepared using the following procedure: 1 g of polyvinyl alcohol (PVA) was dissolved in 10 mL of deionized water under heating and stirring at 95 °C until complete dissolution. After cooling, 1 mL of 1% glutaraldehyde solution was added into the solution under stirring. Subsequently, 1 mL of 1 mol L^{-1} H_2SO_4 solution was mixed with this. The resulting liquid mixture was then coated onto the microdevice and cured to form a PVA/H_2SO_4 gel electrolyte film.

2.7 Characterization

Field emission scanning electron microscopy (VEGA3-SBH, TESCAN) and corresponding energy dispersive spectroscopy (EDX) performed at an accelerating voltage of 20 kV with an electron microscope and transmission electron microscope (Talos F200X, FEI, USA) were employed to observe the morphology, microstructure and distribution of elements of samples. X-ray photoelectron spectroscopy (Supra Axis, Kratos, UK) was utilized to detect the valence states of the elements and the surface chemical composition. Fourier-transform infrared (FTIR) spectroscopy and Raman (DXRxi, Thermo Fisher Scientific, USA) spectroscopy were used to analyze the chemical structures of the prepared materials. X-ray diffraction data were obtained to identify the crystal structure using an X-ray diffractometer (D8 Advance, Bruker, Cu-Kα, $\lambda = 1.5418$ Å, Germany) with Cu Kα radiation.

2.8 Electrochemical measurements

For individual electrodes, the electrochemical performance was examined using a standard three-electrode setup in 1 mol L^{-1} H_2SO_4 electrolyte. The free-standing films directly served as the working electrode, while the counter and reference electrodes consisted of excess activated carbon (AC) and Ag/AgCl in saturated potassium chloride, respectively. A CHI 760E electrochemical workstation was employed for obtaining cyclic voltammetry (CV) curves and electrochemical impedance spectroscopy (EIS) testing. In order to evaluate the long-term stability, the film electrodes and asymmetric microsupercapacitors needed to undergo galvanostatic charge/discharge testing for up to thousands of cycles.

The gravimetric capacitance and volumetric capacitance of single electrodes and CEOG//CWOM AMSCs were calculated from the discharge portion of galvanostatic charge/discharge curves according to eqn (1)–(3):

$$C_g = \frac{I\Delta t}{m\Delta V} \quad (1)$$

$$C_a = \frac{I\Delta t}{S\Delta V} \quad (2)$$

$$C_v = \rho C_g \quad (3)$$

where C_g, C_a and C_v are the gravimetric capacitance (F g^{-1}), area capacitance (mF cm^{-2}) and volumetric capacitance, respectively; I is the current density (mA cm^{-2}); Δt is the discharge time (s); m is the mass of the active substance (mg); ΔV is the voltage window (V); S is the geometric area of the electrode (cm^{-2}); and ρ is the density.

The energy density (E) and power density (P) of the asymmetric microdevice were calculated according to eqn (4) and (5), respectively:

$$E = \frac{1}{2}CV^2 \quad (4)$$

$$P = \frac{E \times 3600}{\Delta t} \quad (5)$$

3. Results and discussion

A schematic diagram illustrating the fabrication process of the all-pseudocapacitive two-dimensional-material-based proton-type asymmetric microsupercapacitor (AMSC) is presented in Fig. 1. Conductive 2D graphene and $Ti_3C_2T_x$ MXene are selected as the pristine target materials to undergo chemical modification based on their inherent structural advantages that can meet the performance indices for constructing high-performance AMSCs. For graphene modification, as displayed in Fig. 1a, graphene oxide (GO) first undergoes rapid volumetric expansion *via* the steam-shock exfoliation of interlayer water molecules under a suddenly rising temperature to produce expanded graphene (EG), significantly enhancing its specific surface area and electron conductivity. Subsequent strong acid treatment introduces abundant electrochemically active oxygen-containing functional groups at an optimized proportion and density on the surface of expanded graphene by regulating the oxidization process of EG to produce expanded-and-oxidized graphene (EOG), augmenting its ion-capturing capabilities to enhance the pseudocapacitive contribution. For $Ti_3C_2T_x$ MXene modification, as displayed in Fig. 1b, delaminated MXene nanosheets with surface termini of –OH, –O and –F serve as the precursor upon selectively etching away the Al layer of the MAX phase and subsequent hand-shaking treatment. This is followed by surface functionalization of the

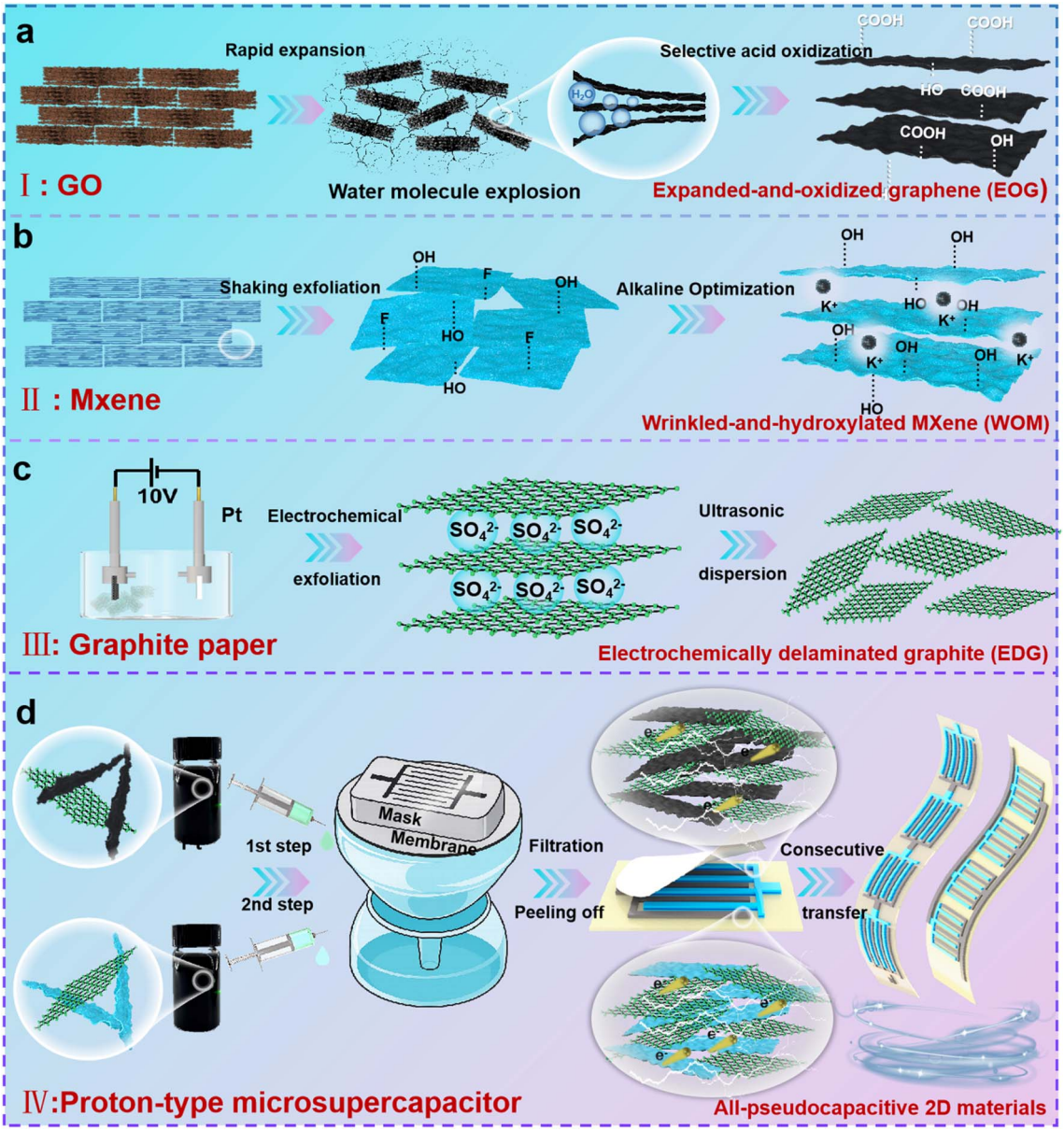

Fig. 1 Schematic illustrations of the design process for a novel proton-type asymmetric microsupercapacitor. (a) The synthesis of acid-functionalized expanded-and-oxidized graphene (EOG), (b) alkali-treated wrinkled-and-hydroxylated MXene (WOM), (c) electrochemically delaminated graphene (EDG), and (d) the all-pseudocapacitive 2D-material-based proton-type asymmetric microsupercapacitor (AMSC).

exfoliated nanosheets with alkali, where KOH is used to regulate the surface termini and introduce more –OH functional groups under alkaline conditions. Meanwhile, the surface becomes wrinkled due to coulombic attraction relating to metal potassium ions, allowing fast ion diffusion and thus forming wrinkled-and-hydroxylated MXene (WOM). To further enhance the electrochemical performance and flexibility of EOG and WOM electrodes, electrochemically delaminated graphite (EDG) is prepared, as displayed in Fig. 1c, in a two-electrode system under a +20 V applied potential to yield a stable and highly conductive EDG dispersion. EDG establishes long-range ordered electron transport pathways, while overlapping the functionalized 2D materials shortens electron diffusion distances and enhances the electrochemical kinetics of the CEOG and CWOG film electrodes. The asymmetric solid-state microsupercapacitor (AMSC) features an EOG cathode and WOG anode with EDG as the conductive additive in both electrodes; it is fabricated by a mask-assisted vacuum filtration method, as displayed in Fig. 1d. The electrode array can be quickly transferred to a flexible polyimide (PI) substrate and coated with H_2SO_4/PVA hydrogel electrolyte, forming an integrated flexible device for wearable electronics applications.

The morphologies of different states of graphene nanosheets, including graphene oxide (GO), expanded graphene oxide (EG), and expanded-and-oxidized graphene (EOG), are presented in Fig. 2a1–c1, respectively. GO powder exhibits

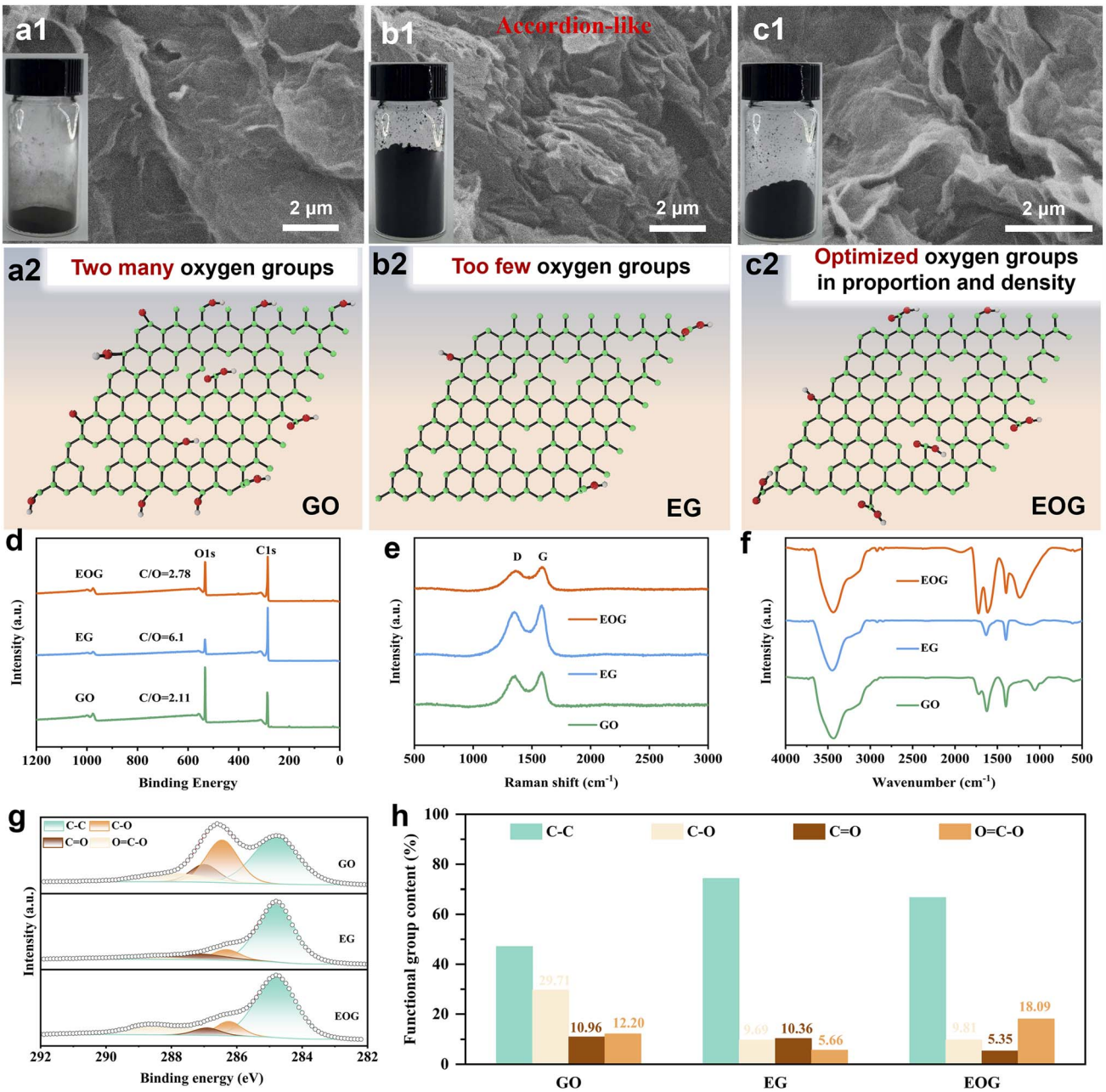

Fig. 2 Morphological and chemical characterization of GO, EG, and EOG powder. SEM images of (a1) GO powder, (b1) EG powder, and (c1) EOG powder. Schematic illustrations of the chemical structure of (a2) GO powder, (b2) EG powder, and (c2) EOG powder. Chemical characterization of GO, EG, and EOG powder: (d) XPS survey spectra, (e) Raman spectra, (f) FTIR spectra and (g) high-resolution C 1s XPS spectra. (h) Relative content of carbon chemical bonds and groups derived from C 1s spectra.

significant agglomeration, while EG powder prepared *via* rapid high-temperature steam-induced expansion displays a novel accordion-like layered morphology with obvious expanded volume from the observation of sample bottles. Upon further acidification, the EOG nanosheets show distinct wrinkles compared to GO, mainly due to keeping a certain extent of π–π stacking after partial oxidization. More detailed features are shown in Fig. S1–S3 at different magnifications. The optical images shown at the bottom-left of Fig. 2a1–c1 clearly demonstrate that, for the same mass, the powder volume decreases in the order EG > EOG > GO. The change in surface functional groups is key for the physical/chemical properties, which is illustrated graphically in Fig. 2a2–c2, and it will be confirmed that the groups experience a change from rich to limited followed by a rearrangement process in the following characterization. These morphological changes further confirm that rapid steam expansion and acid oxidization effectively modulate the microstructure of EOG and enhance its specific surface area. X-ray photoelectron spectroscopy (XPS) analysis, as shown in Fig. 2d, provides evidence of surface chemical changes. The

results show that GO has the lowest C/O atomic ratio (2.11), indicating abundant oxygen-containing groups. After water-steam evaporation and expansion, the C/O ratio of EG increases to 6.1, suggesting that under steam action, surface oxygen-containing groups decompose obviously. Subsequent acidification gradually reduces the C/O ratio of EG from 6.1 to 2.78, indicating the reintroduction of oxygen-containing functional groups onto the EG surface during strong acid treatment. This rearrangement of oxygen-containing functional groups on the EOG surface is beneficial for regulating the electrochemical reaction activity by introducing an optimized proportion and density of active groups. Fig. 2e displays the Raman spectra of the three aforementioned materials, providing supplementary evidence for functional group changes during the expansion and oxidization process. The intensity ratio of the D to G bands (I_D/I_G) first decreases and then increases. This trend corroborates the XPS results, collectively illustrating the transition of the graphitic carbon structure and the introduction of defects.

Fourier-transform infrared (FTIR) spectroscopy analysis of the three materials is shown in Fig. 2f. A broad and strong absorption peak near 3430 cm^{-1} is distinctly observable for all three materials, attributable to O–H stretching vibrations. The intensity of the hydroxyl stretching vibration decreases for EG, evidencing the reduction of hydroxyl groups on GO during the steam thermal expansion process. Upon acidification of EG to yield EOG, the hydroxyl stretching vibration intensity increases slightly. The absorption peak at 1725 cm^{-1} is assigned to the C=O stretching vibrations of carbonyl groups. Compared to GO and EG, the intensity of the carbonyl vibration peak in the further acidified EOG increases obviously. This enhancement is attributed to the restructuring of surface functional groups due to the strong acid regulation of EG nanosheets. X-ray photoelectron spectroscopy (XPS) analysis provided insights into the surface chemical changes, as shown in Fig. 2g. In the high-resolution C 1s XPS spectra, the intensity of the C–C peak first increased and then decreased, which further verifies the change in chemical bonds, indicating the influence of oxygen-containing functional group regulation on the C–C bonds. Based on XPS quantitative analysis of the changes in group species and content shown in Fig. 2h, high proportions of –OH (29.71%), –COOH (12.20%) and –C=O (10.96%) exist in GO, while after expansion and reduction with hot-water steam, the corresponding proportions of groups change to –OH (9.69%), –COOH (5.66%) and –C=O (10.36%). This indicates a decrease in the surface groups in EG and an increase in the carbon content, which is in favor of fast electron transport. Subsequently, after the 6 hour acid treatment of EG, the change in group proportion and density is interesting in EOG, as the –COOH content increases significantly from 5.66% (EG) to 18.09% (EOG), while the –OH content remains relatively constant, changing from 9.69% (EG) to 9.81% (EOG). It is observed that the total content of –COOH and –OH in EG is 15.35%, but the corresponding content for EOG is 27.90%, indicating that the content of effective functional groups markedly increases in EOG. Meanwhile, the ratio between –COOH and –OH increases from 0.58 in EG to 1.84 in EOG, confirming that the main functional groups are also different between EG and EOG. The transformation of groups in terms of proportion and density will be shown to be highly relevant to the pseudocapacitive properties, especially the –COOH change, which can greatly improve the pseudocapacitance due to its strong charge adsorption capacity compared to –OH. Thus, adjusting the expansion and acidification time offers an effective strategy for controlling the proportion and density of surface functional groups on graphene, enabling the selective introduction of oxygen-containing functional groups in favor of pseudocapacitive behavior.

The prepared 2D nanosheets of EOG and EDG are characterized by transmission electron microscopy (TEM), as shown in Fig. 3a and b, respectively. TEM analysis of EOG (Fig. 3a) reveals wrinkled surface morphology and thin sheets. This structural configuration increases the specific surface area of EOG, while the large lateral dimensions of the sheets are beneficial for film forming. TEM analysis of EDG (Fig. 3b) shows flat and large graphene planes with low levels of lattice defects, which can play a key role in enhancing in-plane electrical conductivity due to superior charge-carrier mobility. After the 2D EDG nanosheets are combined with EOG for the CEOG film, the pseudocapacitive charge storage capability of EOG and the composite film flexibility will be enhanced significantly. Optical images of aqueous dispersions (Fig. 3c) demonstrate distinct stability. As can be seen, GO is dispersed readily while EG shows reduced dispersibility after expansion and reduction. This decrease stems from a diminished surface oxygen functional group content, which lowers its hydrophilicity. Subsequent formation of EOG from the acidification of EG increases the oxygen content to some extent, thereby improving the aqueous dispersibility. Surface morphological analysis of CEOG (Fig. 3d) reveals wrinkled EOG sheets uniformly decorated with EDG. EDG acts as an interstitial filler between EOG sheets, establishing an interconnected conductive network that enhances the electrochemical performance. X-ray diffraction (XRD) characterization of CEOG and EDG (Fig. 3e) indicates that EDG has a typical graphite carbon structure, indicating high conductivity for CEOG film. This weakening and the associated peak shifts reflect the presence of defects and inherently reduced crystallinity within the EOG component compared to EDG due to oxidization effects. Energy-dispersive X-ray spectroscopy (EDS) elemental mapping (Fig. 3f) confirms a spatially homogeneous distribution of constituent elements across the material surface. Macroscopic images (Fig. 3g) demonstrate the composite film's excellent flexibility. Stability assessment (Fig. 3h) reveals that the composite film retains structural integrity after undergoing 60 minutes of ultrasonication without any damage.

EOG materials are oxidized with different acidification times of 3 hours, 6 hours, and 9 hours, and then the electrochemical properties of the free-standing CEOG film electrodes are tested. It is shown in Fig. 4a that after 6 hours of acidification and oxidization, the CV area of CEOG-6 is significantly larger than those of samples treated for 3 hours and 9 hours, as well as the untreated EG sample, which is attributed to the regulation of the surface functional group content. As shown in Fig. S4, the CV curve of EG with an obviously smaller CV area does not

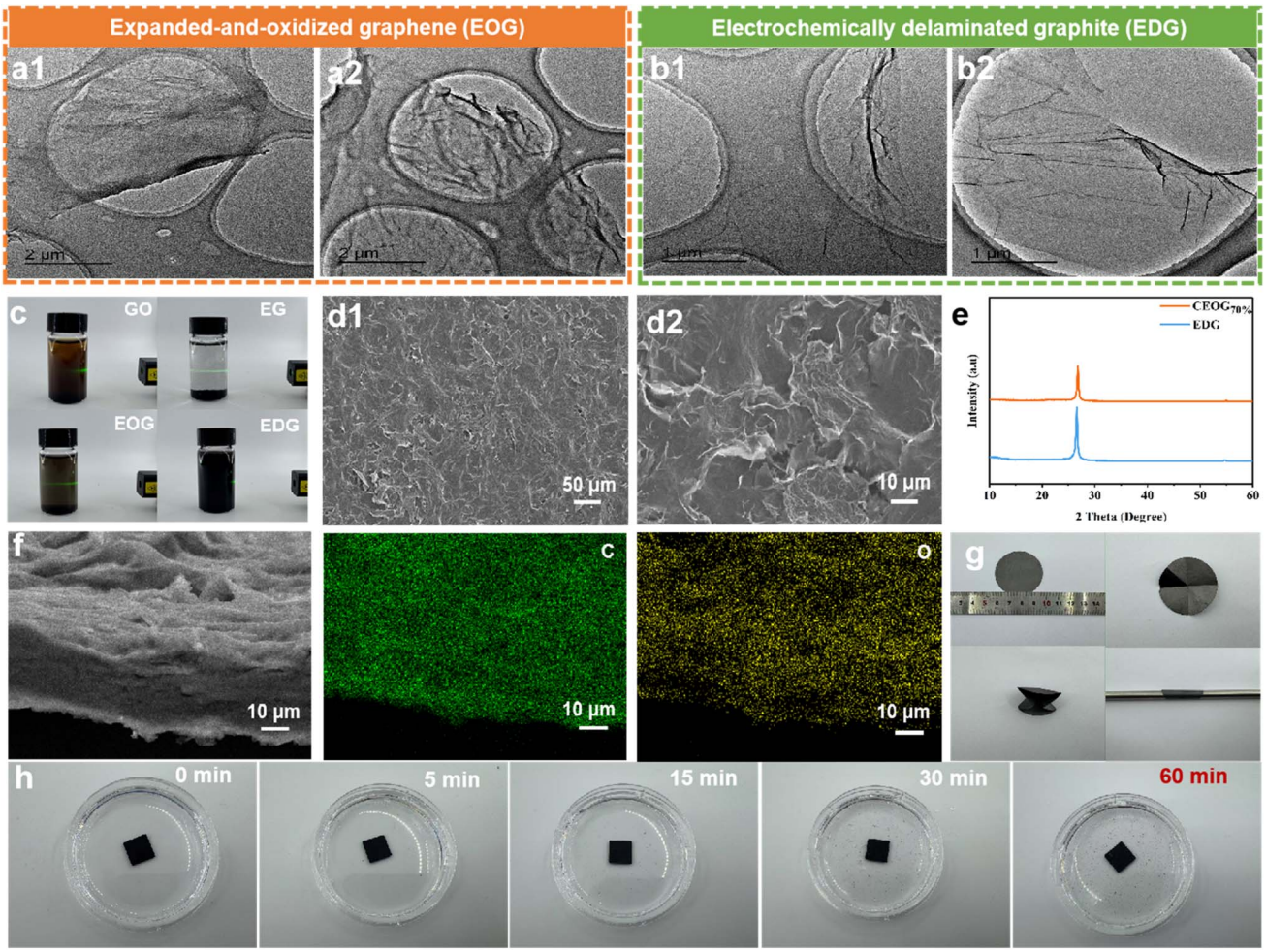

Fig. 3 Morphological and chemical characterization of free-standing CEOG film. (a1 and a2) TEM images of EOG. (b1 and b2) TEM images of EDG. (c) Aqueous dispersions of GO, EG, EOG, and EDG. (d1 and d2) SEM images of the CEOG surface. (e) XRD patterns of CEOG and EDG films. (f) Elemental mapping images of CEOG film. (g) The flexibility of CEOG film and (h) a demonstration of the stability of CEOG film after different periods of ultrasonic treatment.

exhibit distinct redox peaks, unlike those of the acid-treated sample, indicating that –COOH groups provide a higher pseudocapacitive contribution, as there are more –COOH groups on the EOG surface compared to EG nanosheets. The Nyquist plots in Fig. 4b reveal low series resistance (R_s) and charge transfer resistance (R_{ct}), suggesting good interfacial conductivity and efficient charge transport processes at the selected oxidization times. Next, Fig. 4c compares the mass specific capacitance values at different current densities. It can be seen that CEOG with 6 hours of acidification exhibits a higher capacity compared to those with 3 hours and 9 hours of acidification because appropriate functional groups are established during this oxidization time. Meanwhile, EDG plays an important role in determining the electrochemical behavior, which can be seen from the comparison among EDG, EOG and CEOG electrodes shown in Fig. S5. When the EOG : EDG ratio is 7 : 3, the area of the CV curve is significantly increased. The specific capacitance has been enhanced due to the excellent lateral conductivity of the large 2D EDG nanosheets, improving the carrier transport in the CEOG film electrode. This also can be confirmed based on Fig. S6, as the Nyquist plot reveals that $CEOG_{70\%}$ has low R_s and R_{ct}, suggesting good interfacial conductivity and efficient charge-transport processes. When the ratio of EOG in CEOG film electrodes is raised to 80% and 90%, the capacitive performance is still inferior to the $CEOG_{70\%}$ electrode at different current densities (Fig. S7). Therefore, the above experiments have proved that 6 hours of acidification with the addition of 70% EDG is the optimal condition for CEOG electrodes for the following further studies. CV curves of CEOG at different scan rates are shown in Fig. 4d, and they have a pair of obvious reversible peaks. Also, as shown in Fig. 4e, the GCD curves have a relatively long platform during the charging and discharging process, indicating superior pseudocapacitive behavior. As shown in Fig. 4f, the mass specific capacitance is up to 382 F g^{-1} at 1 mA cm^{-2} and remains at 167 F g^{-1} at a high current density of 50 mA cm^{-2}. Next, the electrochemical kinetics are first analyzed based on the capacitive contributions (k_1v) and diffusion-controlled contributions ($k_2v^{1/2}$), as shown in Fig. 4g. As the scan rate continuously increases, the capacitive contribution increases from 40% to 83%, while the diffusion

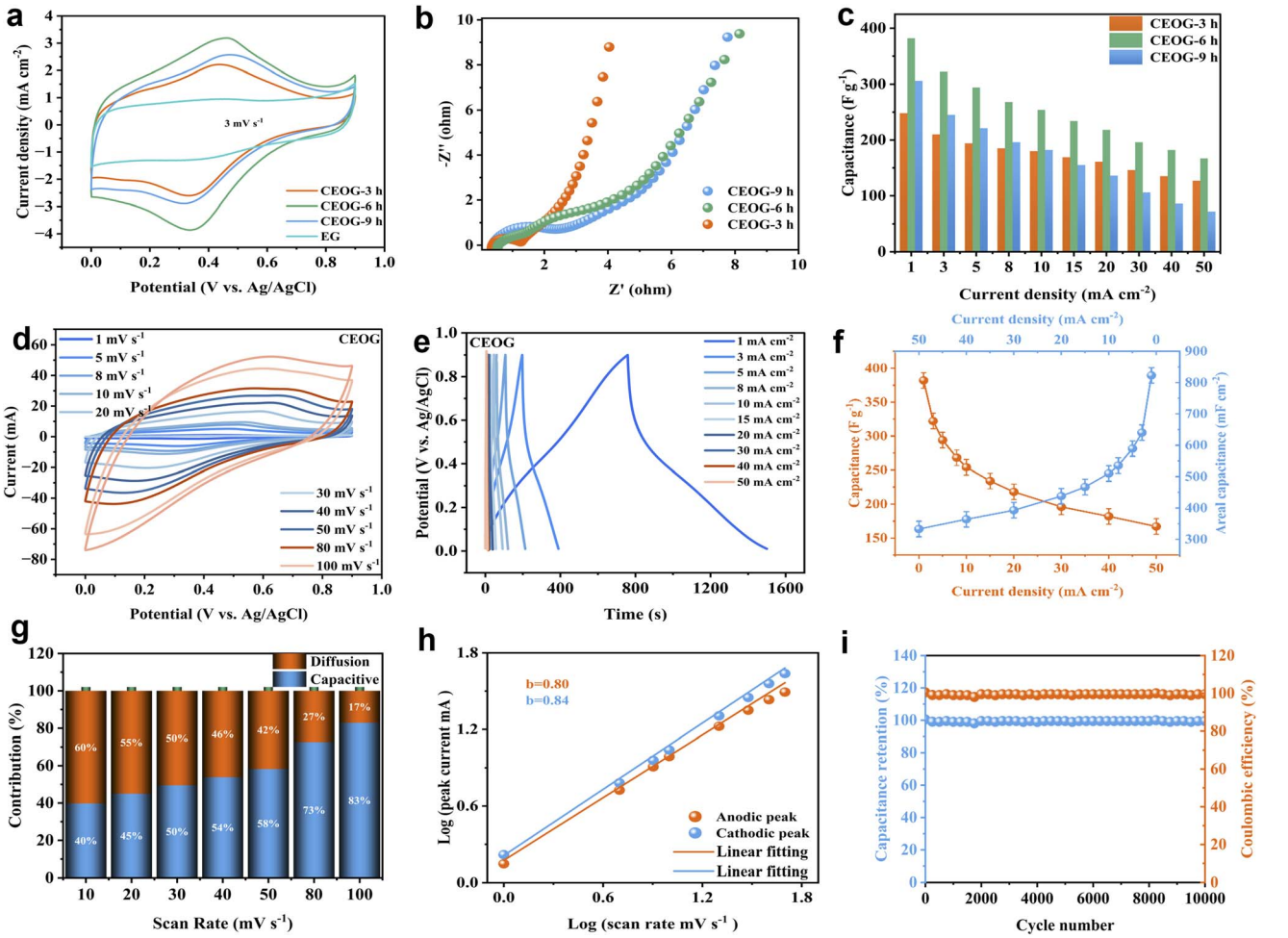

Fig. 4 Electrochemical performance analysis of CEOG and EG film electrodes. (a) CV curves of CEOG film with acidification times of 3 hours, 6 hours, and 9 hours for EOG. (b) EIS curves of different CEOG electrodes. (c) The capacitance properties of different CEOG electrodes. (d) CV curves of the optimal CEOG electrode. (e) GCD curves of CEOG. (f) Gravimetric and areal capacitances of CEOG. (g) Pseudocapacitive contributions of the CEOG electrode at various scan rates. (h) *b*-Value analysis of the CEOG electrode. (i) Long-term cycling performance of the CEOG electrode.

contribution decreases from 60% to 17%, confirming the dominant role of capacitive behavior at higher rates. The *b* fitting values for the cathodic and anodic peaks are 0.84 and 0.80, respectively, indicating capacitive-dominated behavior due to the *b* value being close to 1. Long-term stability testing is conducted based on 10 000 charging/discharging cycles. Impressively, the capacity retention is almost 100% without any attenuation, demonstrating high stability in acidic aqueous electrolyte, benefiting from the covalent groups on the graphene surface.

Regarding the anode material, as shown in Fig. 5a, the successful etching of Ti_3AlC_2 yields delaminated MXene nanosheets without impurities following the hand-shaking method. XPS was employed to characterize and analyze the surface chemical composition and chemical states of the electrode material. The survey spectrum (Fig. 5b) confirms the presence of Ti, C, O, K and F elements in the WOM sample. The appearance of a K 2p peak in the WOM film indicates the successful intercalation of potassium into the MXene interlayers. The binding energy of the K $2p_{3/2}$ peak at approximately 292.7 eV is consistent with the formation of K–Ti–F bonds, providing indirect evidence for chemical interactions between potassium and the MXene framework. The C 1s spectrum revealed positive shifts (toward higher binding energies) in the peaks corresponding to C–Ti, C–Ti–O, C–O, and O–C=O bonds after KOH treatment, signifying a decrease in the electron cloud density. Similarly, the Ti 2p spectrum showed positive shifts for both spin–orbit doublet peaks (including the Ti $2p_{1/2}$ orbital) from a metallic to an oxidized state. These observed increases in binding energy are attributed to electrostatic interactions between the intercalated K^+ ions and the negatively charged terminal groups on the MXene sheets. Obviously, from the O 1s spectrum displayed in Fig. 5f, abundant –OH terminals are formed on the WOM surface, indicating successful hydroxyl substitution due to the alkalization treatment. Fig. 5g presents an optical photograph of the CWOM film electrode. Fig. 5h and i shows SEM images of the film surface at various magnifications, revealing the presence of wrinkles. These wrinkles result from the combined

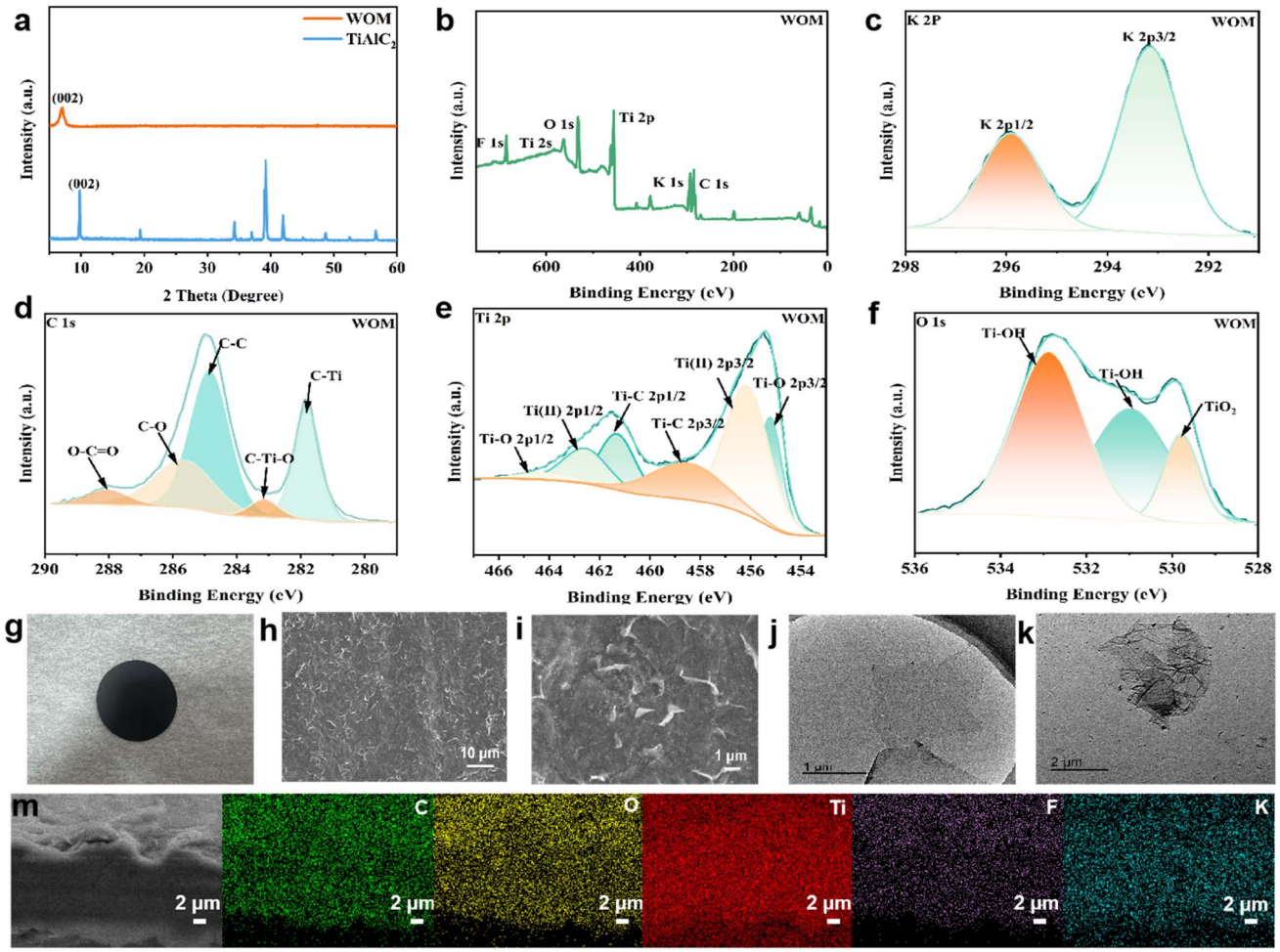

Fig. 5 Morphological and chemical characterization of WOM materials and free-standing CWOM films. (a) The XRD patterns of WOM and $TiAlC_2$. (b) The XPS survey spectrum of WOM. (c) K 2p, (d) C 1s, (e) Ti 2p and (f) O 1s high-resolution XPS spectra. (g) A photograph of CWOM. (h and i) SEM images of the CWOM film surface. (j) A TEM image of MXene. (k) A TEM image of WOM. (m) EDS analysis of CWOM.

effects of K^+ intercalation and hydroxyl group modification of the MXene, leading to the formation of crumpled MXene. TEM analysis is conducted on both pristine MXene and WOM. Pristine MXene exhibits the characteristics of large size and a flat surface (Fig. 5j). However, after alkalization treatment it is evident that the originally thin layers undergo curling around the edges of the MXene nanosheets under the influence of the alkali, forming a wrinkled structure (Fig. 5k). Finally, EDS elemental analysis was performed on the synthesized alkalized MXene (Fig. 5m). The results demonstrate the homogeneous distribution of C, O, Ti, F, and K elements across the CWOM film electrode, confirming the successful preparation and synthesis of the CWOM electrode material.

To further investigate the electrochemical performance of MXene and CWOM, CV and GCD tests were employed. Fig. 6a–c compares the GCD curves of CWOM and pristine MXene electrodes at different current densities. At identical current densities and active mass loadings, the CWOM film electrode exhibits more pronounced redox plateaus in its GCD curves. As shown in Fig. 6c, at a current density of 3 mA cm^{-2}, CWOM displays significantly longer charge–discharge times than pristine MXene. The enhanced pseudocapacitive contribution during the charging/discharging process for CWOM is related to the highly active surface of WOM nanosheets with more active oxygen terminal groups. To further analyze the electrochemical energy storage behavior, CV tests were performed on CWOM. As depicted in Fig. 6d, the shapes of the oxidation and reduction peaks are similar, with no significant peak distortion, indicating fast reaction kinetics in CWOM. The modulated surface functional groups and the wrinkled surface are beneficial for the electrochemical reactions of WOM. A comparison of the specific mass capacitance and areal capacitance values is presented in Fig. 6e and f. The discharge specific capacitance values of CWOM at current densities of 3, 5, 10, 15, 20, 30, 40, and 50 mA cm^{-2} are 550, 474, 350, 293, 262, 236, 229, and 227 F g^{-1}, respectively. In contrast, pristine MXene exhibits discharging specific capacitance values of 356, 295, 238, 207, 185, 151, 125, and 106 F g^{-1} at the same current densities. These results demonstrate that alkalized MXene possesses obviously higher specific capacitance compared to pristine MXene. Nyquist plots reveal low R_s and R_{ct} values (Fig. 6g), suggesting good interfacial conductivity and efficient charge transport

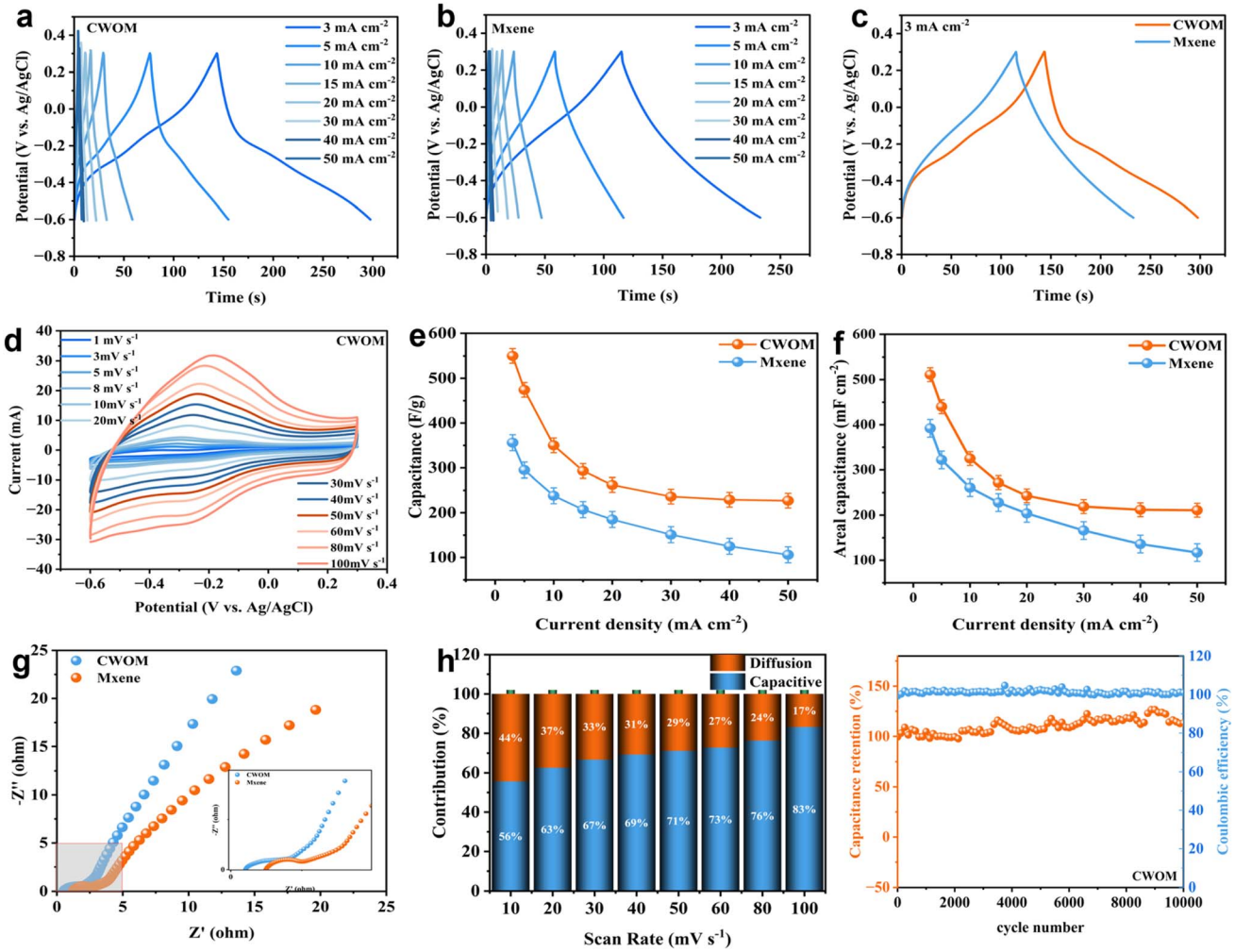

Fig. 6 Electrochemical properties of MXene and free-standing CWOM film electrodes. (a) GCD curves of CWOM. (b) GCD curves of MXene. (c) A comparison of the GCD curves of MXene and CWOM film electrodes at 3 mA cm^{-2}. (d) CV curves of CWOM at various current densities. (e) A comparison of gravimetric capacitance. (f) A comparison of areal capacitance. (g) EIS plots of CWOM and MXene film electrodes. (h) Pseudocapacitive contributions of CWOM at various scan rates. (i) Long-term cycling of the CWOM film electrode at 10 mA cm^{-2}.

processes, which enable high-power output under high current conditions. The pseudocapacitive contribution is also fitted, as shown in Fig. 6h and S8. As the scan rate continuously increases, the capacitive contribution increases from 56% to 83%, while the diffusion contribution decreases from 44% to 17%, confirming the dominant role of capacitive behavior at higher rates. Fig. 6i shows that after 10 000 consecutive charging/discharging cycles at a current density of 10 mA cm^{-2}, the capacity of CWOM shows no decay, demonstrating excellent stability. This remarkable stability is attributed to the beneficial modification of surface covalent functional groups and the stabilizing effect of K^+ intercalation in the molecular interlayers.

Given that both positive CEOG and negative CWOM demonstrate excellent electrochemical performance, a solid-state proton-type asymmetric microsupercapacitor (AMSC) is constructed, denoted as CWOM//CEOG. The total active material loading is around 2 mg cm^{-2}. A schematic illustration of the pseudocapacitive contribution mechanism of the prepared conductive 2D materials in the assembled AMSC is presented in Fig. 7a. The AMSC has unique characteristics, such as all-pseudocapacitive 2D nanosheets, a more ion-accessible wrinkled active surface, and so on, which are beneficial for its electrochemical behavior. As shown in Fig. 7b, the assembled AMSC achieved a maximum operating voltage of 1.5 V, significantly widening the voltage window and laying the foundation for achieving a high energy density. Fig. 7c and d displays the CV and GCD curves of the AMSC device, respectively. The shapes of the curves show no significant distortion or deformation with clear redox peaks and charging/discharging platforms, indicating stable and reversible electrochemical behavior over a wide operating voltage range. As depicted in Fig. 7e, both the R_s and R_{ct} values are small, demonstrating good electronic conductivity and fast charge transfer processes in these conductive positive and negative 2D materials, enabling a high power output under high current conditions. As shown in Fig. 7f, the AMSC delivers a high specific capacitance of 91 F g^{-1} at a current density of 3 mA cm^{-2}, corresponding to an areal capacitance of 151.2 mF cm^{-2}, demonstrating

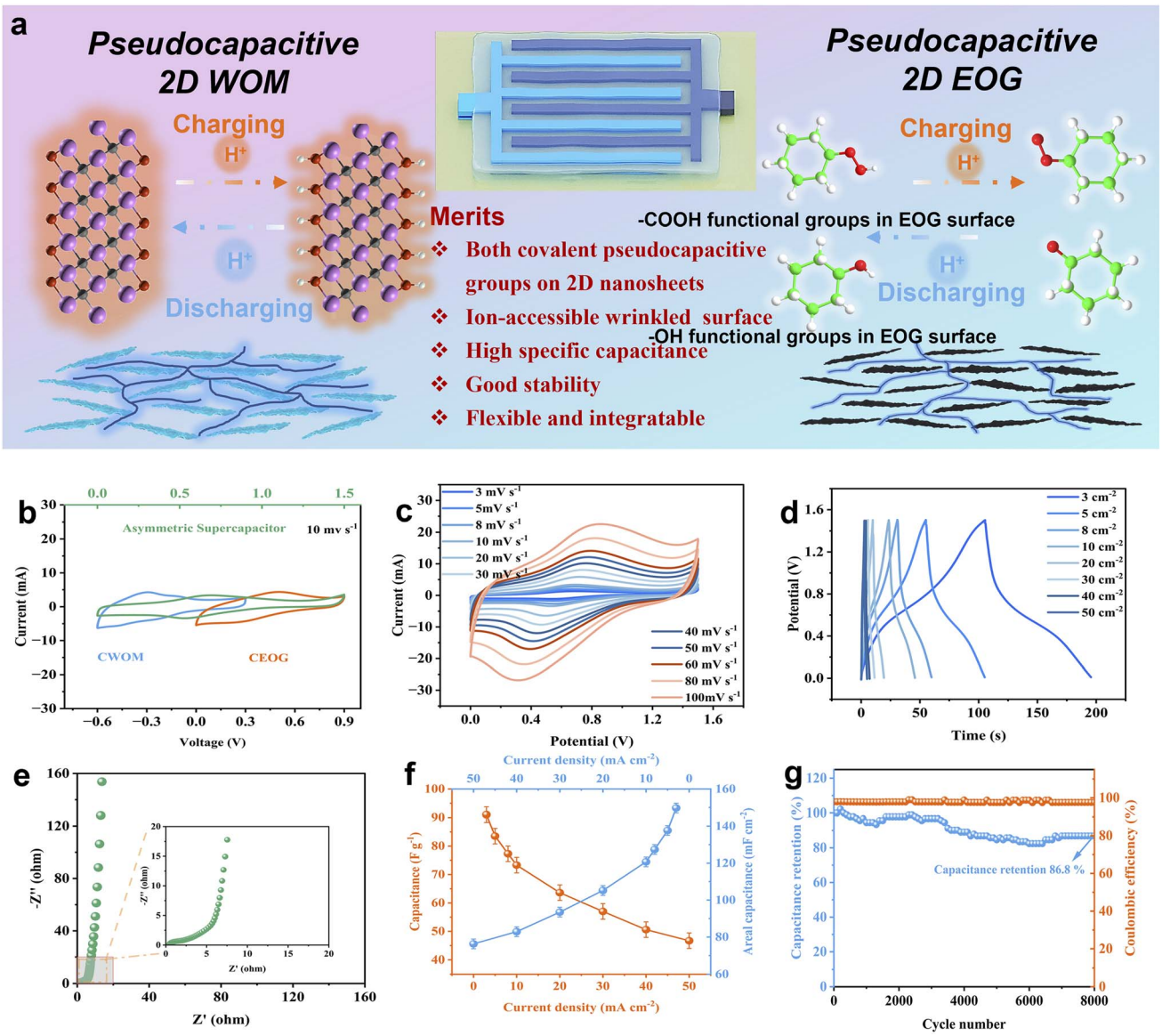

Fig. 7 Electrochemical properties of the assembled proton-type CWOM//CEOG AMSC. (a) A schematic illustration of the pseudocapacitive contribution mechanism in the AMSC device. (b) CV curves of the AMSC at 10 mV s^{-1}. (c) CV curves of the AMSC at various scan rates. (d) GCD curves of the AMSC at various current densities. (e) The Nyquist plot. (f) Gravimetric and areal capacitances of the AMSC device. (g) Long-term cycling stability testing.

outstanding energy storage capabilities. From the stability testing shown in Fig. 7g, the device exhibits exceptional stability over 8000 charging/discharging cycles with 86.8% initial capacitance retention and ~100% coulombic efficiency.

To meet the demands of flexible electronics, microsized energy storage devices should possess high energy density and stability, and have flexible and integrable characteristics. The flexibility and integrability of the fabricated AMSC device are first evaluated, as shown in Fig. 8a–c. Under various bending conditions, the interdigitated electrodes in the AMSC show no signs of detachment or fracture. By solid phase transfer with the assistance of the PI substrate with strong adhesion, an array of integrable ASMCs was able to be interconnected on the PI substrate. A surface SEM image (Fig. 8d) reveals distinct boundaries (~500 μm) between adjacent interdigitated electrodes, effectively preventing short circuits. As shown in Fig. 8e–g, a multimeter is used to test the conductivity and short-circuiting of the prepared asymmetric ASMC in an intuitive way. Fig. 8h and i shows that the CV curves measured at different bending angles (0°, 45°, 90°, and 180°) are nearly identical, indicating excellent capacity retention under mechanical deformation. To fulfil the variable voltage requirements of diverse electronic products, devices are connected in series and in parallel, and they show different degrees of expanded voltage windows and discharging ability depending on the number of interconnected AMSCs (Fig. 8j and k). To evaluate the power density and energy density of the assembled AMSC, the Ragone plot (energy density *vs.* power density) is

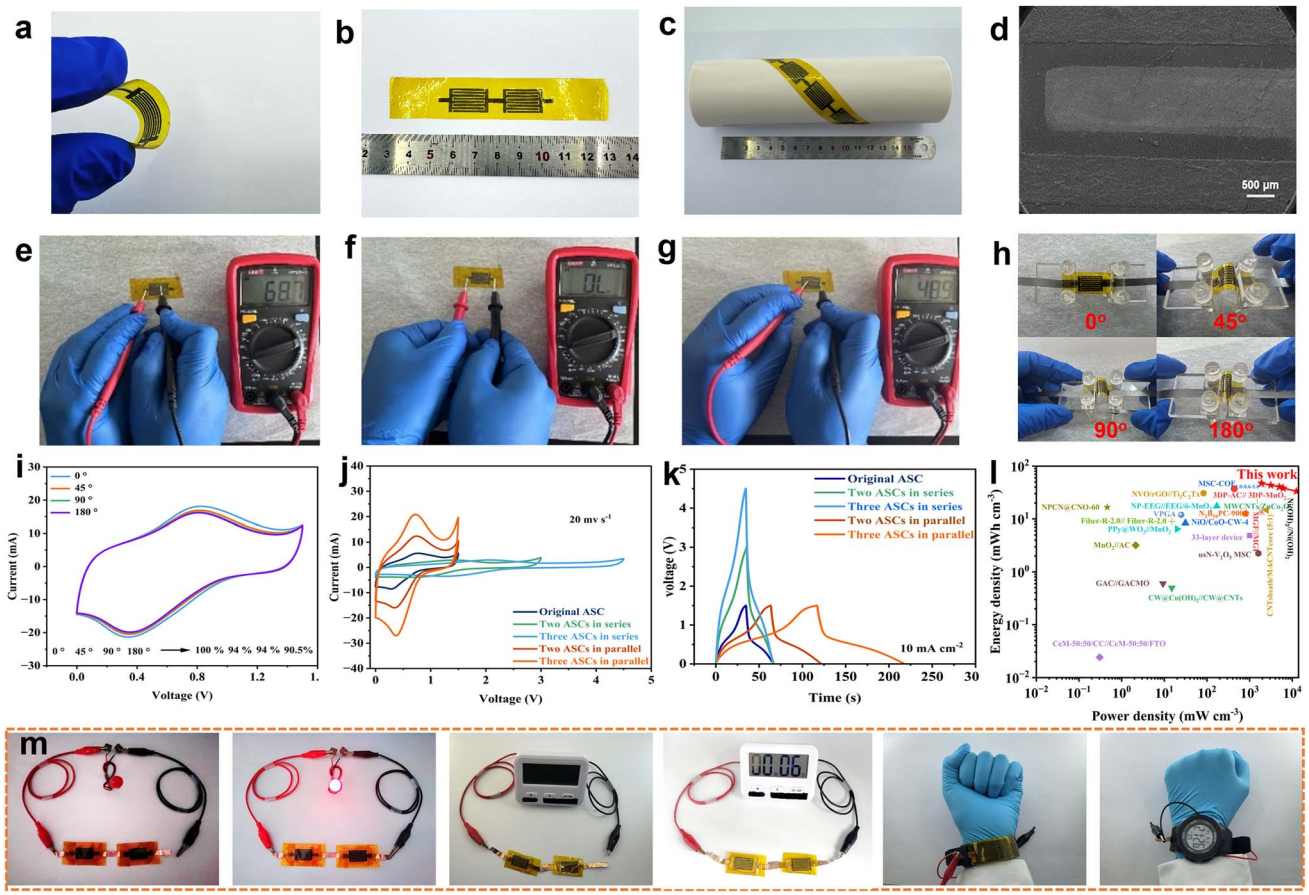

Fig. 8 A demonstration of the application potential of the flexible and integrable AMSC device. (a–c) A series of optical images of the prepared AMSC. (d) An SEM image of the microelectrodes in the AMSC. (e–h) Resistance measurements from an interdigital electrode in the AMSC. (h) Angled bending tests. (i) CV curves at different bending angles. (j) CV curves from AMSCs connected in series and in parallel (10 mV s^{-1}). (k) GCD curves from AMSCs connected in series and in parallel at 10 mA cm^{-2}. (l) A Ragone plot. (m) Demonstrations of various applications.

presented in Fig. 8l and S9, alongside a comparison with other reported devices. The microsupercapacitor exhibits a high volumetric energy density of up to 47.25 mW h cm^{-3} (23.62 W h kg^{-1}) at a power density of 1900.55 mW cm^{-3} (950.27 W kg^{-1}), which outperforms many previously reported high-performance supercapacitors, including 3DP-AC//3DP-MnO_2 (1.9 V, 37.3 mW h cm^{-3}),[31] NiO/CoO-CW-4 (1.0 V, 8.38 mW h cm^{-3}),[32] CW@$Cu(OH)_2$//CW@CNTs (1.5 V, 0.496 mW h cm^{-3}),[33] CeM-50:50/CC//CeM-50 : 50/FTO (2.0 V, 0.024 mW h cm^{-3}),[34] CNTsheath/M-kCNTcore (5 : 1) (1.0 V, 14.7 mW h cm^{-3}),[35] PPy@WO_3//MnO_2 (2.4 V, 6.5 mW h cm^{-3}),[36] usN-V_2O_5 MSC (1.0 V, 2.25 mW h cm^{-3}),[37] NPCN@CNO-60 (0.6 V, 16.57 mW h cm^{-3}),[38] N_2B_{10}PC-900 (1.7 V, 12.6 mW h cm^{-3}),[39] VPGA (1.0 V, 11.9 mW h cm^{-3})[40] and those listed in Table S1. Compared to MXene-based state-of-the-art micro-supercapacitors, such as interdigitated patterned MXene MSCs (0.6 V, 41.9 mW h cm^{-3}),[41] N,S-MXene MSCs (0.6 V, 8.9 mW h cm^{-3}),[42] MXene/PH1000 (0.6 V, 9.4 mW h cm^{-3}),[43] NaNVO@C10/rGO//MXene AFSIC (1.7 V, 35 mW h cm^{-3}),[44] MAT5 FSC (0.8 V, 26.8 mW h cm^{-3}),[45] and CNC/MXene (0.8 V, 11.3 mW h cm^{-3}),[46] the designed CWOM//CEOG AMSC is strongly competitive. In order to show its application potential, various practical scenarios are demonstrated in Fig. 8m. Two serially connected AMSCs can successfully power an LED lamp and an electronic timer. Serially connected AMSCs can power an electronic watch, even in a bent state, highlighting the device's huge potential for use in flexible and wearable electronics.

4. Conclusions

In summary, an advanced asymmetric solid-state proton-type pseudocapacitor is developed by integrating modified negative MXene (WOM) and positive graphene (EOG) materials with optimized active surface covalent groups through the strategy of acid oxidation and alkaline optimization. An interesting expanded-and-oxidized process is used to produce the active EOG nanosheets with pseudocapacitive oxygen-containing functional groups at an appropriate proportion and density on the graphene basal plane. After the process, the –COOH content changes significantly, as the –COOH content increases from 5.66% (EG) to 18.09% (EOG), while the –OH content remains relatively constant. Meanwhile, the ratio of –COOH to –OH is changed from 0.58 in EG up to 1.84 in EOG, which is shown to be considerably beneficial for greatly improving the

pseudocapacitance due to the strong charge adsorption capacity compared to –OH. Upon the surface functionalization of the exfoliated MXene materials with alkali, wrinkled terminal-optimized nanosheets are obtained with more active –OH functional groups and fast ion transport channels. With the assistance of EDG nanosheets with large 2D lateral dimensions and high electron conductivity, the resulting flexible positive CEOG electrode and negative CWOM electrode achieve high specific capacitances of 382 F g^{-1} and 550 F g^{-1}, respectively, along with excellent long-term cycling stability without any visible attenuation. Benefiting from the synergistic design involving surface chemistry engineering and an all-pseudocapacitive configuration, the assembled flexible solid-state proton microsupercapacitor exhibits an extended voltage window of 1.5 V, delivering a high energy density of 47.25 mW h cm^{-3} (23.62 W h kg^{-1}) at a power density of 1900.55 mW cm^{-3} (950.27 W kg^{-1}) and retaining 86.8% of its initial capacity after 8000 charge/discharge cycles. This work demonstrates the potential of rationally engineered conductive 2D materials and makes them competitive as reliable candidates for use in next-generation flexible microsized energy storage devices.

Author contributions

Y. W. supervised the project and wrote the original draft of the manuscript. J. W. performed all the experiments. J. D. and X. X. oversaw sample preparation. H. S. and L. Y. conceptualized the work. X. L. and Z. L. revised the manuscript.

Conflicts of interest

The authors declare no competing financial interests.

Data availability

The data supporting this article have been included as part of the supplementary information (SI). Supplementary information is available. See DOI: https://doi.org/10.1039/d5sc07080e.

Acknowledgements

This work was supported by the National Nature Science Foundation of China (No. 52402126), Shaanxi Provincial High-level Youth Talent Introduction Program (No. 202102430), Qinchuangyuan introducing high-level innovation and entrepreneurship talent projects (No. QCYRCXM-2022-343) and the Research Start-up Fund of Shaanxi University of Science & Technology (No. 126022224).

References

1 K. Guo, Y. Wan, N. Yu, L. Hu, T. Zhai and H. Li, *Energy Storage Mater.*, 2018, **11**, 144–151.
2 H. Luo, F. Li, M. Wang, S. Sun, M. Zhou, W. Zhang, H. Guo, X. Su, X. Li and L. Ma, *Chem. Sci.*, 2025, **16**, 753–760.
3 P. Zhang, F. Wang, S. Yang, G. Wang, M. Yu and X. Feng, *Energy Storage Mater.*, 2020, **28**, 160–187.
4 H. Luo, D. Su, S. Yang, Y. Li, Z. Shan, M. Zheng, M. Hong, T. Liu and M. Lu, *Nano Energy*, 2025, **139**, 110973.
5 T. Bashir, S. Zhou, S. Yang, S. A. Ismail, T. Ali, H. Wang, J. Zhao and L. Gao, *Electrochem. Energy Rev.*, 2023, **6**, 5.
6 S. Yang, Q. Gao, Y. Li, H. Cai, X. Li, G. Sun, S. Zhuang, Y. Tong, H. Luo and M. Lu, *J. Energy Chem.*, 2024, **93**, 24–31.
7 D. Du, H. Chen, S. Sun, L. Zeng, Z. Wu, H. He, X. Li and C. Zhang, *ACS Appl. Mater. Interfaces*, 2025, **17**, 32362–32372.
8 M. Pantrangi, E. Ashalley, M. K. Hadi, H. Xiao, Y. Zhang, W. Ahmed, N. Singh, A. Alam, U. Younis, F. Ran, P. Liang and Z. Wang, *Energy Storage Mater.*, 2024, **73**, 103791.
9 J. Hao, L. Yuan, B. Johannessen, Y. Zhu, Y. Jiao, C. Ye, F. Xie and S.-Z. Qiao, *Angew. Chem., Int. Ed.*, 2021, **60**, 25114–25121.
10 J. Hao, S. Zhang, H. Wu, L. Yuan, K. Davey and S.-Z. Qiao, *Chem. Soc. Rev.*, 2024, **53**, 4312–4332.
11 Y. Wu, W. Shuang, Y. Wang, F. Chen, S. Tang, X.-L. Wu, Z. Bai, L. Yang and J. Zhang, *Electrochem. Energy Rev.*, 2024, **7**, 17.
12 C. Zhao, L. Shan, R. Sun, X. Wang and F. Ding, *Mater. Today*, 2024, **81**, 104–117.
13 N. Lan, Y. Shen, J. Li, H. He and C. Zhang, *Adv. Mater.*, 2025, **37**, 2412989.
14 N. Lan, J. Li, L. Zeng, D. Luo, D. Du, X. Li, H. He and C. Zhang, *Adv. Mater.*, 2025, 2419528.
15 X. Xu, Z. Lu, L. Hua, J. Dong, Z. Guo, Y. Kou, J. Wu, H. Yu and Y. Wang, *J. Colloid Interface Sci.*, 2025, **679**, 643–655.
16 J. Dong, L. Hua, Z. Lu, F. Xie, X. Xu, Z. Guo, J. Wu and Y. Wang, *Energy Storage Mater.*, 2024, **72**, 103686.
17 J. Zhang, N. Kong, S. Uzun, A. Levitt, S. Seyedin, P. A. Lynch, S. Qin, M. Han, W. Yang, J. Liu, X. Wang, Y. Gogotsi and J. M. Razal, *Adv. Mater.*, 2020, **32**, 2001093.
18 X. Li, Y. Wu, T. Chen, Q. Wang, C. Lu, H. Hao, B. Wei, H. Wang, C. Yao, F. Zhang, H. Pang and G. Wang, *Chem. Eng. J.*, 2025, **519**, 164816.
19 X.-L. Li, D.-D. Han, Y.-C. Zhang, H. Zhou, T.-T. Zhang, L. Wang and Y.-L. Zhang, *Adv. Funct. Mater.*, 2025, **35**, 2423854.
20 M. Gao, F. Wang, S. Yang, A. Gaetano Ricciardulli, F. Yu, J. Li, J. Sun, R. Wang, Y. Huang, P. Zhang and X. Lu, *Mater. Today*, 2024, **72**, 318–358.
21 H. Luo, X. Su, Z. Chen, H. Guo, R. Zhao, Q. Gao, M. Lu and T. Liu, *Adv. Mater.*, 2025, 2507978.
22 Q. Jiang, N. Kurra, M. Alhabeb, Y. Gogotsi and H. N. Alshareef, *Adv. Energy Mater.*, 2018, **8**, 1703043.
23 C. Wang, F. Liu, J. Chen, Z. Yuan, C. Liu, X. Zhang, M. Xu, L. Wei and Y. Chen, *Energy Storage Mater.*, 2020, **32**, 448–457.
24 J. Zhu, L. Wang, X. Gan, T. Tang, F. Qin, W. Luo, Q. Li, N. Guo, S. Zhang, D. Jia and H. Song, *Energy Storage Mater.*, 2022, **47**, 158–166.
25 K. Akada, S. Obata and K. Saiki, *Carbon*, 2022, **189**, 571–578.
26 H. Luo, H. Guo, X. Li, S. Li, Y. Li, J. Shi, Q. Gao, H. He, M. Lu, Q. Zhang and D. Chao, *Matter*, 2025, 102379.
27 R. Kumar, S. Sahoo, E. Joanni, R. K. Singh, K. Maegawa, W. K. Tan, G. Kawamura, K. K. Kar and A. Matsuda, *Mater. Today*, 2020, **39**, 47–65.
28 Y. Peng, Z. Chen, R. Zhang, W. Zhou, P. Gao, J. Wu, H. Liu, J. Liu, A. Hu and X. Chen, *Nano-Micro Lett.*, 2021, **13**, 192.

29 Z. Zhang, B. Tan, L. Xie, Z. Han, H. Quan and D. Chen, *Appl. Catal., B*, 2025, **379**, 125703.
30 C. Zhang, Q. Fan, J. Xu, M. Huang, F. Luo, D. Wang and Z. Zheng, *Chem. Eng. J.*, 2025, **505**, 159162.
31 L. Zeng, W. Kang, X. Liu, H. He, X. Li and C. Zhang, *Carbon*, 2025, **232**, 119761.
32 W. Xiong, L. Zhao, J. Ouyang, Y. Tian, L. Wang, M. Li, Y. Wang, M. Cheng, Q. Sheng, Z. Li, J. Luo and Y. Luo, *J. Colloid Interface Sci.*, 2025, **679**, 243–252.
33 Q. Zhang, H. Li, Y. Xu, X. Su, J. Yu, J. Sui, L. Yu and L. Dong, *Diamond Relat. Mater.*, 2024, **150**, 111732.
34 M. M. Momeni, F. Mohammadinejad, F. Ghasemipur and B.-K. Lee, *J. Alloys Compd.*, 2025, **1029**, 180761.
35 C. Chen, *Chem. Eng. J.*, 2025, **520**, 165708.
36 Z. Huang, M. Zhang, W. Zhou, D. Li, Y. Li, X. Hao and J. Xu, *J. Energy Storage*, 2025, **117**, 116179.
37 H. Raha, N. Dey and P. K. Guha, *J. Energy Storage*, 2025, **128**, 117177.
38 D. Zheng, Y. Lai, M. Wang, C. Gong, Q. Li, H. Xie, Q. Bai and C. Zhang, *Appl. Surf. Sci.*, 2025, **696**, 162995.
39 Z. Liu, X. Cui, X. Yang, W. Jiang, Z. Yuan, J. Wan, Y. Liu and F. Ma, *J. Power Sources*, 2025, **630**, 236118.
40 C. Zhang, F. Yang, Y. Ma, Y. You, Z. Yang, Y. Zhang, Z. He, Y. Zhang, Z. Yong, Y. Cao and Q. Li, *Chem. Eng. J.*, 2025, **505**, 159353.
41 E. Kim, J. Song, T.-E. Song, H. Kim, Y.-J. Kim, Y.-W. Oh, S. Jung, I.-S. Kang, Y. Gogotsi, H. Han, C. W. Ahn and Y. Lee, *Chem. Eng. J.*, 2022, **450**, 138456.
42 P. Sun, J. Liu, Q. Liu, J. Yu, R. Chen, J. Zhu, G. Sun, Y. Li, P. Liu and J. Wang, *Chem. Eng. J.*, 2022, **450**, 138372.
43 J. Ma, S. Zheng, Y. Cao, Y. Zhu, P. Das, H. Wang, Y. Liu, J. Wang, L. Chi, S. Liu and Z. S. Wu, *Adv. Energy Mater.*, 2021, **11**, 2100746.
44 F. Ma, L. Li, X. Chen, X. He, Q. Li, J. Sun, R. Jiang, Z. Lei and Z.-H. Liu, *Adv. Funct. Mater.*, 2025, 2506540.
45 J. Zhou, H. Dai, H. Wang, W. Zhao, Y. Wang, H. Xu, T. Cheng, L. Yin, T. Zhang, Y. Guo, J. Zhou and G. Sun, *Small*, 2025, **21**, 2502658.
46 Y. Wang, T. Xu, J. Qi, A. Wang, K. Liu, M. Zhang, W. Huan, Y. Meng, S. Tong, C. Zheng, H. Xiang, J. Li and C. Si, *Adv. Compos. Hybrid Mater.*, 2024, **7**, 120.